ACS APPLIED MATERIALS & INTERFACES

www.acsami.org

Research Article

Wearable Textile Supercapacitors for Self-Powered Enzyme-Free Smartsensors

Tongrui Sun,[§] Liuxue Shen,[§] Yu Jiang, Junlin Ma, Fengjuan Lv, Hongting Ma, Dawei Chen, and Nan Zhu*

Cite This: *ACS Appl. Mater. Interfaces* 2020, 12, 21779–21787

Read Online

ACCESS | Metrics & More | Article Recommendations | Supporting Information

ABSTRACT: Wearable energy storage and flexible body biomolecule detection are two key factors for real-time monitoring of human health in a practical environment. It would be rather exciting if one wearable system could be used for carrying out both energy storage and biomolecule detection. Herein, carbon fiber-based $NiCoO_2$ nanosheets coated with nitrogen-doped carbon (CF@$NiCoO_2$@N−C) have been prepared via a simple electrochemical deposition method. Interestingly, being a dual-functional active material, CF@$NiCoO_2$@N−C exhibits excellent behaviors as a supercapacitor and prominent electrocatalytic properties, which can be applied for enzyme-free biosensor. It exhibits outstanding energy storage, high capacitive stability (94% capacitive retention after 10,000 cycles), and pre-eminent flexible ability (95% capacitive retention after 10,000 bending cycles), as well as high sensitivity for enzyme-free glucose detection (592 μA mM^{-1}). Moreover, the CF@$NiCoO_2$@N−C-based wearable supercapacitors would be used as self-powered energy systems for enzyme-free biosensors. Integrating with bluetooth, we have successfully developed a wearable self-powered enzyme-free smartsensor, remotely controlled using a smartphone for health monitoring in a practical environment. From this prospective study, it was found that the design of wearable self-powered smartsensors, demonstrating energy storage and enzyme-free biosensing in one system, provides a promising device for detecting body biomolecules, which has the potential to be implemented in the artificial intelligent fields.

KEYWORDS: *$NiCoO_2$, dual-functional materials, wearable supercapacitors, enzyme-free smartsensors, self-powered energy systems, wearable sensors*

1. INTRODUCTION

Rapid development of wearable electronic devices has been improving human daily life in areas, such as medical treatment,[1] protection,[2−4] health monitoring,[5−7] flexible energy supply systems,[8−11] and artificial intelligence.[12] Currently, wearable biosensing systems are attracting the attention of researchers because of their excellent portability and wide application in health monitoring. Generally, a stable wearable energy supply and a facile universal material are two challenges for fabricating a wearable biosensing system for large-scale applications. Thus, wearable energy device-powered sensors should be developed and studied for further enhancing the flexibility and sensing performance. The energy-harvesting technologies for wearable systems based on solar cells,[13] piezoelectrics,[14] and triboelectrics[15] have been extensively investigated. Considering the demand of flexibility and safety for wearable energy storage devices, conventional batteries are not suitable because of their bulk volume, heavy weight, and rigidity, and it is difficult to satisfy the rapid-charging conditions of wearable electronic devices.[16−18]

Supercapacitors, as one of the promising energy storage devices, have attracted great attention in the wearable electronic field because of their fast charging/discharging ability and long cycle life. In addition, the emerging all-solid-state supercapacitors could easily meet the needs of flexibility and various deformations (e.g. bending and twisting) as the wearable electronic devices.[19−22] Meanwhile, energy storage performance is also a key factor affecting the use of wearable devices. Today, the integrated systems of supercapacitors because of these advantages have been attracting widespread attention.[23−25] Dahiya et al. designed a graphene-based flexible self-charging power pack that can collect light energy in a supercapacitor and then power the CuO-based pH sensor to detect pH changes.[26] However, the graphene-based supercapacitors possessed a low energy density, impacting the performance of pH sensors further limiting their application in wearable devices. Nowadays, carbon materials mainly domi-

Received: March 24, 2020
Accepted: April 23, 2020
Published: April 23, 2020

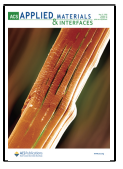

https://dx.doi.org/10.1021/acsami.0c05465
ACS Appl. Mater. Interfaces 2020, 12, 21779−21787

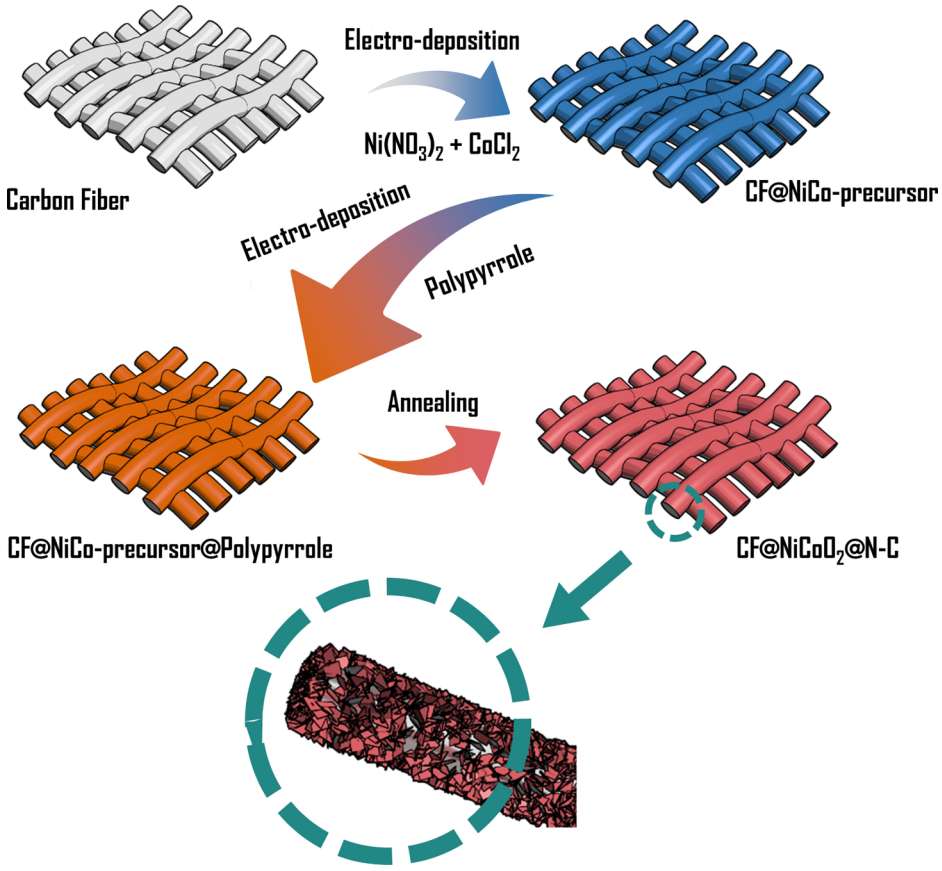

Figure 1. Schematic illustration of preparing $CF@NiCoO_2@N-C$

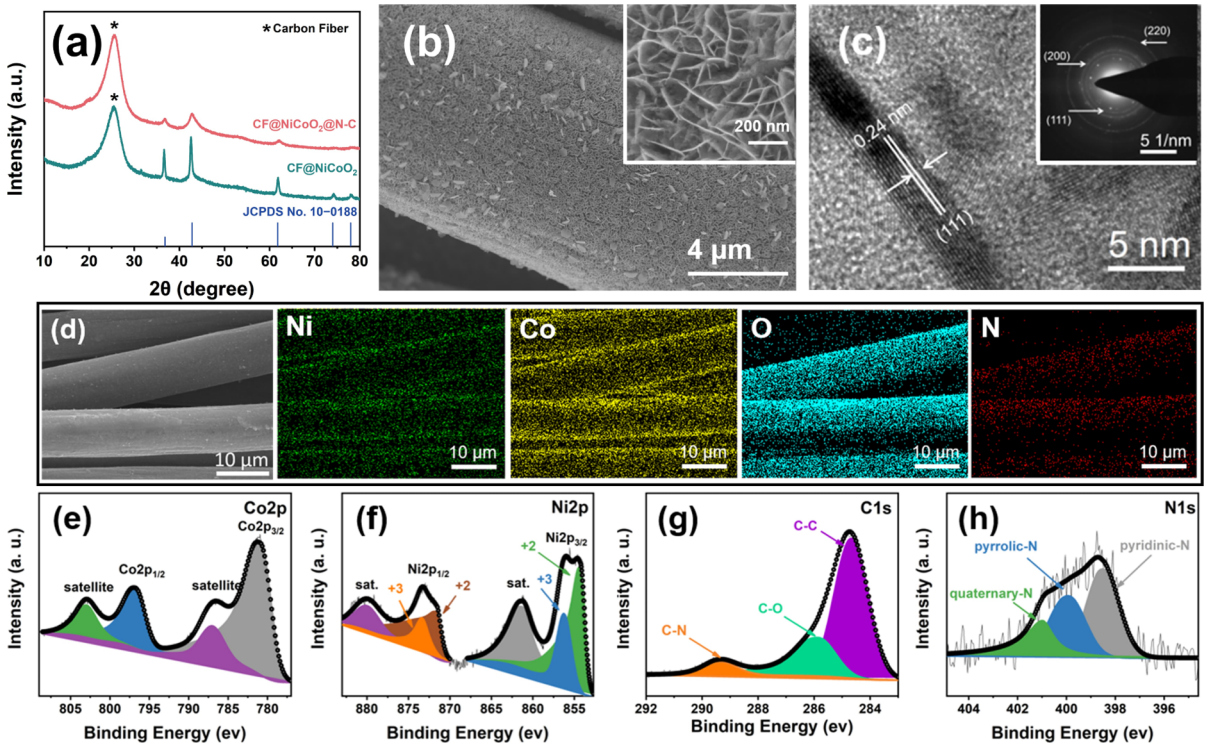

Figure 2. (a) XRD patterns of the $CF@NiCoO_2@N-C$ nanosheets and $CF@NiCoO_2$; (b) SEM image of $CF@NiCoO_2@N-C$ nanosheets, the inset is the corresponding enlarged SEM images; (c) HRTEM image of the $CF@NiCoO_2@N-C$ nanosheets, the inset is the SAED pattern of the nanosheets; (d) EDX map of the $CF@NiCoO_2@N-C$ nanosheets; and the XPS spectra of the $CF@NiCoO_2@N-C$ nanosheets; (e) Co 2p spectrum; (f) Ni 2p spectrum; (g) C 1s spectrum; and (h) N 1s spectrum.

https://dx.doi.org/10.1021/acsami.0c05465
ACS Appl. Mater. Interfaces 2020, 12, 21779−21787

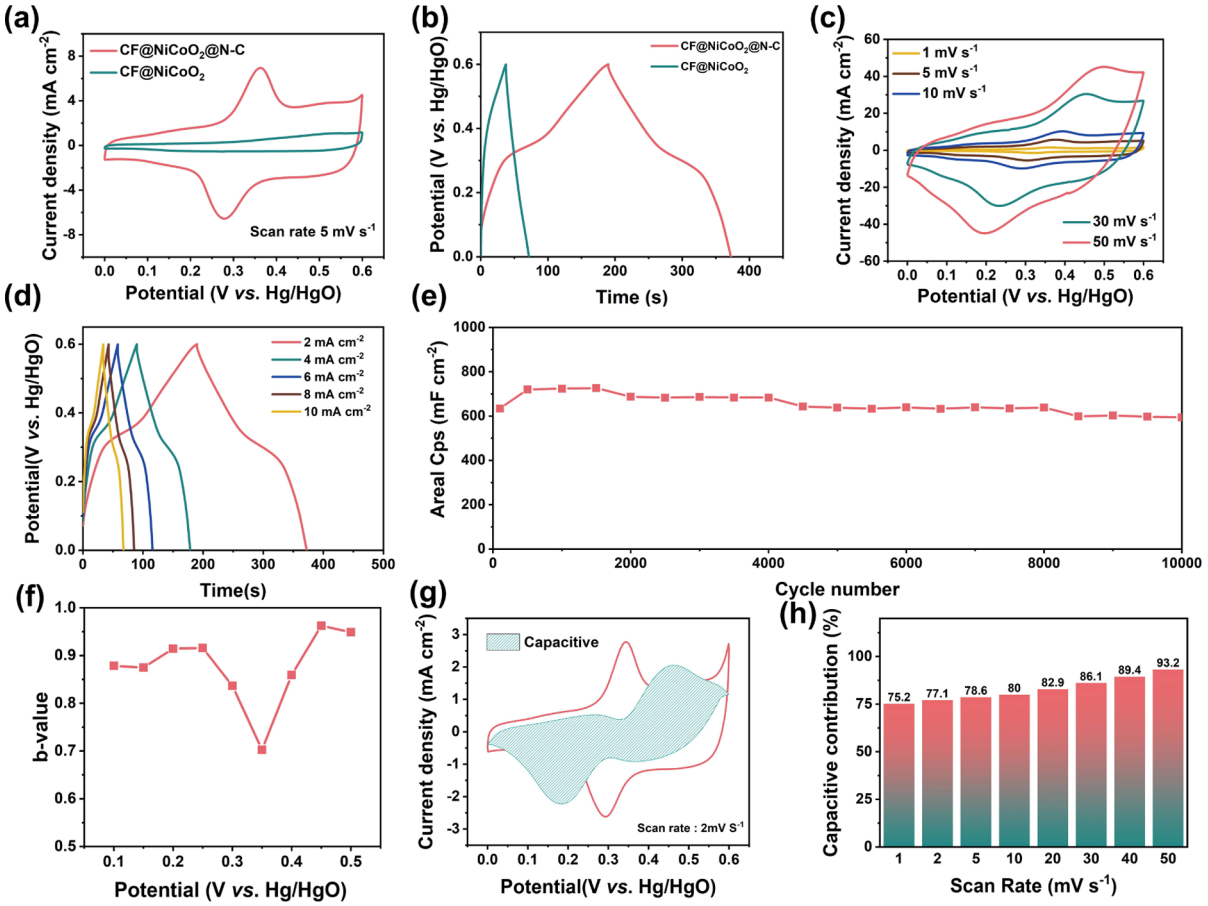

Figure 3. (a) CV curves of CF@$NiCoO_2$@N−C (red) and CF@$NiCoO_2$ (aquamarine) at 5 mV s^{-1}; (b) GCD curves of CF@$NiCoO_2$@N−C and CF@$NiCoO_2$ at 2 mA cm^{-2}; (c) CV curves of CF@$NiCoO_2$@N−C at different scan rates from 1 to 50 mV s^{-1}; (d) GCD curves of CF@$NiCoO_2$@N−C at different current densities; (e) the cycling performance of CF@$NiCoO_2$@N−C; (f) *b*-values of CF@$NiCoO_2$@N−C; (g) the separation of capacitive and diffusion currents of CF@$NiCoO_2$@N−C at a scan rate of 2 mV s^{-1}; (h) the contribution ratio of capacitive and diffusion-controlled processes at different scan rates.

nate the industrial market of conventional capacitors because of their excellent stability,[27,28] but their inherent low energy density limit their application in wearable areas. Transition metal oxide materials with high theoretical specific capacitance, rich redox reaction sites, and low cost have been regarded as a class of promising materials for supercapacitors.[29−32] Among them, nickel−cobalt oxide ($NiCoO_2$) has been conceived as a promising scalable alternative because of its advantages of excellent energy storage performance, abundant resources, and environmental friendliness.[33,34] Importantly, $NiCoO_2$ is also an economical and facile candidate material for non-enzymatic biosensors,[35,36] compared with traditional enzyme biosensor materials.

Herein, we developed a nitrogen-doped and carbon-coated $NiCoO_2$-based dual-functional electrode for simultaneous application in wearable supercapacitors and enzyme-free glucose sensors. The as-obtained CF@$NiCoO_2$@N−C for supercapacitors exhibited pre-eminent electrochemical performance including a high specific capacitance (644 mF cm^{-2} at 2 mA cm^{-2}) and a long stable cycling performance (retaining 94% after 10,000 cycles). Interestingly, flexible asymmetric supercapacitors were assembled using the CF@$NiCoO_2$@N−C electrode, and the obtained full-cell exhibited excellent electrochemical behaviors with long cycling and bending performances, which would be a potential device for practical wearable use. Meanwhile, the CF@$NiCoO_2$@N−C electrode could also be used in a wearable enzyme-free sensor for glucose monitoring with a high sensitivity of 500 μA mM^{-1}. This wearable dual-functional device made of the CF@$NiCoO_2$@N−C electrode would be used as a self-powered energy system for biosensors. After integrating with portable workstations and bluetooth, wearable enzyme-free sensors could be remotely controlled using a smartphone for health monitoring. Therefore, the design of a wearable self-powered smartsensor system, demonstrating energy harvesting, energy storage, and enzyme-free sensing in one system, would be a promising system for detecting body biomolecules and has the potential to be implemented in the artificial intelligent fields.

2. RESULTS AND DISCUSSION

2.1. Materials Fabrication and Characterization. The schematic of the preparation of CF@$NiCoO_2$@N−C nanosheets on a CF substrate is depicted in Figure 1. The CF@NiCo-precursor@polypyrrole (PPy) was first *in situ* grown on the CF via the two steps of electrodeposition and then annealed in an Ar atmosphere. The detailed process was discussed in the Experimental Section.

The crystal structure of the as-prepared samples was determined using the X-ray diffraction (XRD) pattern (Figure 2a). The diffraction peaks at 36.7, 42.8, and 62.2° well correspond to the (111), (200), and (220) planes of $NiCoO_2$ (JCPDS no. 10-0188), while the diffraction peaks at 25.34 and

https://dx.doi.org/10.1021/acsami.0c05465
ACS Appl. Mater. Interfaces 2020, 12, 21779−21787

43.1° can be indexed to the CF.[37] The low crystallinity of CF@$NiCoO_2$@N−C was because of the addition of nitrogen and carbon. The scanning electron microscopy (SEM) images of CF@$NiCoO_2$@N−C showed that nanosheets were uniformly grown on the CF (Figure 2b). The 3D-nanostructure has more active sites and structural stability. Moreover, there appeared collapsed CF@$NiCoO_2$ without coating PPy on the surface in control (Figure S1). The structure of the CF@NiCo-precursor was similar to that of CF@$NiCoO_2$@N−C (Figure S2). It indicated that the addition of nitrogen-doped carbon (N−C) protected the nanosheet structure during the annealing process. The structure and lattice fringes of the CF@$NiCoO_2$@N−C nanosheets were further revealed by high-resolution transmission electron microscopy (HRTEM) characterization (Figure 2c). A clear lattice fringe of 0.24 nm well matched with the (111) plane of $NiCoO_2$ (JCPDS no. 10-0188). The selected area electron diffraction (SAED) patterns showed obvious rings matching with the (111), (200), and (220) planes of $NiCoO_2$ (the inset of Figure 2c), and these data well correspond to the XRD results. Meanwhile, the uniform distribution of Ni, Co, O, and N on the CF is displayed in the energy dispersive spectroscopy (EDS) map (Figure 2d), which would provide larger areas of electroactive sites and space to store electrolyte ions.

The detailed electronic states of the CF@$NiCoO_2$@N−C nanosheets were further characterized using the X-ray photoelectron spectrum (XPS) shown in Figure 2e−h. In Figure 2e, the peaks at 780.9 and 796.7 eV can be indexed to Co^{2+}. The high-resolution Ni 2p spectrum (Figure 2f) showed two spin−orbit doublets characteristic of Ni^{2+} and Ni^{3+}, as well as two shake-up satellite peaks. The fitting peaks at 854.2 and 871.6 eV were indexed to Ni^{2+}, while the peaks at 856.2 and 873.3 eV can be indexed to Ni^{3+}.[33,38] The ratio of Ni^{3+}/Ni^{2+} shows that the majority of nickel is Ni^{2+}, while the existence of the Ni^{3+} component would be confirmed by a signal appearing for the defect site. In the C 1s spectrum of CF@$NiCoO_2$@N−C (Figure 2g), the peaks at 284.6 and 285.8 eV can be indexed to the bonding configurations of C═C and C−C, respectively. Especially, a small peak at 289.3 eV, ascribed to C−N, suggests that nitrogen was doped into the carbon surface. Moreover, the N 1s spectrum in Figure 2h was used to determine the nitrogen configurations. The three individual peaks were indexed to pyridinic N (398.5 eV), pyrrolic N (400.1 eV), and quaternary N (401.1 eV). It can be expected that sufficient doping of pyridinic N and pyrrolic N would induce numerous extrinsic defects and active sites for rapid ion diffusion, which thus greatly enhanced the electrochemical performance.[39,40]

2.2. Electrochemical Properties of CF@$NiCoO_2$@N−C. The electrochemical performance of the CF@$NiCoO_2$@N−C nanosheets has been investigated. In order to prove the excellent performance of the as-prepared CF@$NiCoO_2$@N−C nanosheets, they were compared with CF@$NiCoO_2$ using the results of cyclic voltammetry (CV) test (Figure 3a). The CF@$NiCoO_2$@N−C showed clear redox peaks at around 0.35 and 0.28 V during the electrochemical process, while CF@$NiCoO_2$ aggregated easily and cannot take part in the redox reaction efficiently (Figure 3a blue line).[33] In particular, there appeared a larger CV area of CF@$NiCoO_2$@N−C, indicating a large capacitance. The galvanostatic charge/discharge (GCD) curves were also obtained for CF@$NiCoO_2$@N−C and CF@$NiCoO_2$ (Figure 3b). In addition, the GCD curves of CF@$NiCoO_2$ at different current densities and CV curves at different scan rates were obtained as well (Figure S3). CF@$NiCoO_2$@N−C showed a longer discharge time indicating a larger specific capacitance, because of the additional active sites for the redox reaction. This result corresponded well with the CV results, showing a better electrochemical performance of CF@$NiCoO_2$@N−C. Furthermore, the CV curves of CF@$NiCoO_2$@N−C with various scan rates are shown in Figure 3c. The clear redox peaks could be observed, which were mainly ascribed to the reversible reactions between metal ions (Ni and Co) and hydroxyl ions (OH^-). The corresponding faradaic reactions could be described using eqs 1−4.[41,42]

$$NiO + OH^- \leftrightarrow NiOOH + e^- \quad (1)$$

$$CoO + OH^- \leftrightarrow CoOOH + e^- \quad (2)$$

$$CoOOH + OH^- \leftrightarrow CoO_2 + H_2O + e^- \quad (3)$$

$$NiOOH + OH^- \leftrightarrow NiO_2 + H_2O + e^- \quad (4)$$

There was an apparent pair of redox peaks, implying the abundant changes in the valence states and diffusion behaviors. Upon increasing the scan rate, the anodic peaks shifted toward a higher potential, while the cathodic peaks shifted toward a lower potential, which were ascribed to the polarization effects of the electrode. GCD measurements were carried out at different current densities to estimate the capacitances of the CF@$NiCoO_2$@N−C (Figure 3d). The specific capacitances were evaluated to be 644, 606, 577, 556, and 536 mF cm^{-2}, corresponding to the current densities of 2, 4, 6, 8, and 10 mA cm^{-2}, respectively. Importantly, the specific capacitance at a high current density of 10 mA cm^{-2} still maintained around 85% of the initial value at 2 mA cm^{-2}. These results confirmed that the introduction of nitrogen-doped carbon greatly enhanced the supercapacitor performance at a high current density.

To further understand the ion diffusion of the materials, electrochemical impedance spectroscopy (EIS) measurement was performed and the results are shown in Figure S4. The *X*-axis intercept in the high frequency range revealed equivalent series resistance (R_S), composed of the ionic resistance of the electrolyte, electronic resistance of the electrode materials, and interface resistance.[43] The R_S values of CF@$NiCoO_2$@N−C and CF@$NiCoO_2$ were 1.9 and 2.2 Ω, respectively. The smaller R_S value indicated a higher conductivity of the CF@$NiCoO_2$@N−C electrode and a better contact between the electrode and the substrate. Furthermore, the straight line of CF@$NiCoO_2$@N−C was steeper in the low-frequency region, because the addition of nitrogen-doped carbon greatly improves the conductivity of the active materials.[44] Moreover, the stability performance of the CF@$NiCoO_2$@N−C positive electrode is shown in Figure 3e. There remained about 94% capacitance after 10,000 cycles at a high rate of 10 mA cm^{-2}, and it continued increasing for the first 100 cycles because of the gradual activation of the reactive materials.[45,46] Thus, the structures of CF@$NiCoO_2$@N−C possessed good stability during the redox reaction, and nitrogen-doped carbon greatly increased the electrode conductivity and provided more electroactive sites.

The superior rate capability of CF@$NiCoO_2$@N−C drew the attention to understand the kinetics mechanism and the dominating process during the electrochemical reaction. CV curves were analyzed at various scan rates according to eq 5.[47,48]

https://dx.doi.org/10.1021/acsami.0c05465
ACS Appl. Mater. Interfaces 2020, 12, 21779−21787

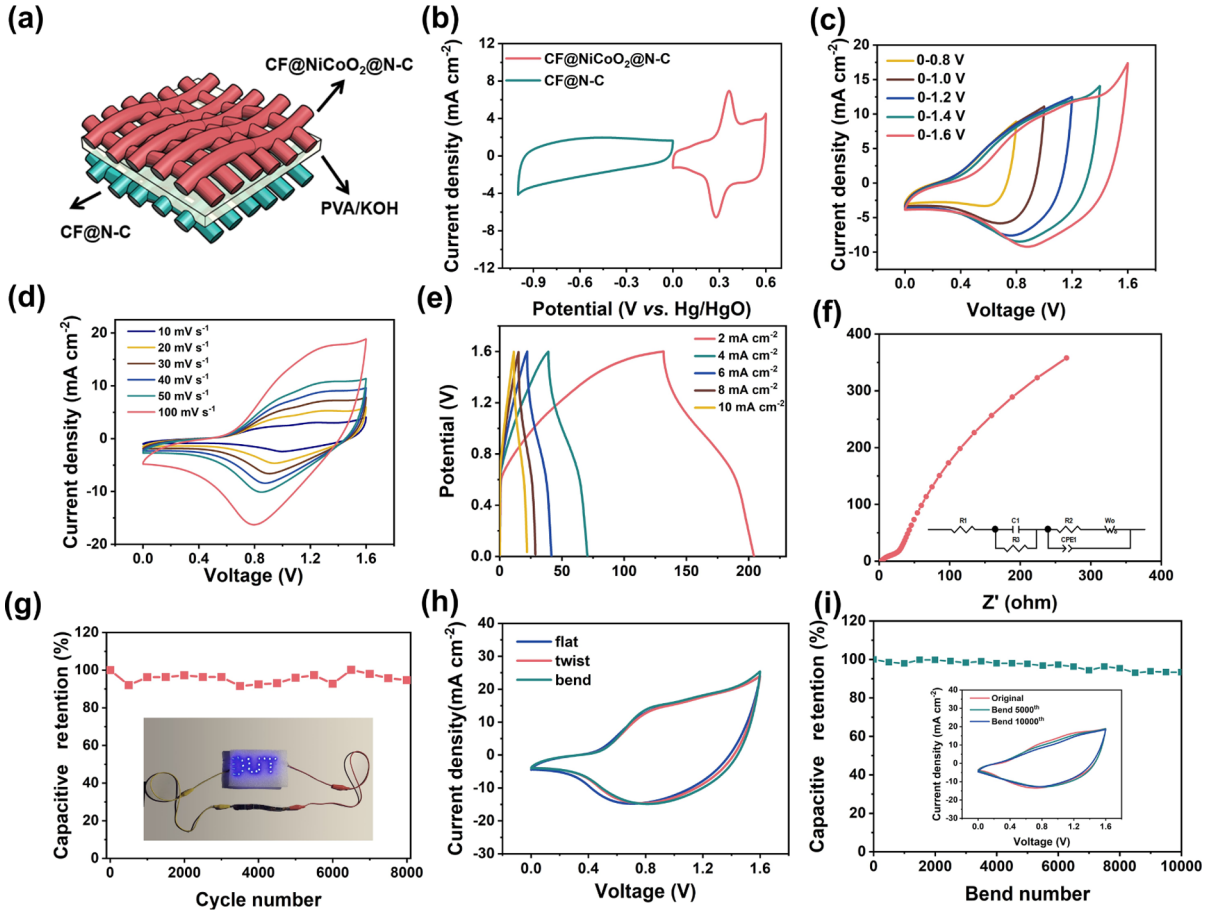

Figure 4. (a) Schematic diagram of FASC; (b) CV curves of CF@NiCoO$_2$@N−C and CF@N−C at 5 mV s^{-1}; (c) CV curves of FASC at 10 mV s^{-1} over a voltage range from 0−1.0 to 0−1.6 V; (d) CV curves of the FASC at different scan rates from 10 to 100 mV s^{-1}; (e) GCD curves of the FASC at different current densities; (f) EIS data of the FASC; (g) the cycling performance of the FASC, the inset is blue DUT LEDs powered by the FASC; (h) the stability of the FASC under straight, bending and twisting states at 100 mV s^{-1}, respectively; (i) bending stability of the FASC after 10,000 cycle testing, the inset is the CV curves of the FASC after bending of 0, 5000, and 10,000 cycles.

$$i = a\nu^b \quad (5)$$

where i was the current, ν was the scan rate, a and b were the constants. In the equation, a b-value of 0.5 indicated a diffusion-controlled process, whereas a b-value of 1 indicated a surface-capacitance process. The b-values of CF@NiCoO$_2$@N−C at different potentials are shown in Figure 3f. A b-value of 0.7 was obtained at a peak potential of 0.35 V, indicating that the process was mostly diffusion-controlled. Meanwhile, b-values in the range of 0.8−1.0 were obtained at potentials higher or lower than 0.35 V, indicating that the process was dominantly capacitive controlled.

Further studies were carried out to quantitatively distinguish the capacitive contributions at various scan rates using the CV curves. The current response can be divided into a combination of two mechanisms: surface-capacitive processes and diffusion-controlled processes, as depicted in eq 6[49,50]

$$i(V) = k_1\nu + k_2\nu^{1/2} \quad (6)$$

where i was the current under a fixed potential (V), k_1 and k_2 were constants. In eq 6, $k_1\nu$ and $k_2\nu^{1/2}$ represent the current of the surface-capacitive contribution and the diffusion-controlled contribution, respectively. The percentage of capacitive contribution at a fixed potential was quantitatively determined by the diffusion-controlled contribution and capacitive contribution, and a 77.1% capacitive contribution was obtained at 2 and 1 mV s^{-1} (Figures 3g and S5). Meanwhile, upon increasing the scan rate from 1 to 50 mV s^{-1}, the capacitive contribution increases, indicating that the surface-capacitive process dominated the electrochemical reaction at high scan rates (Figure 3h). As a result, the excellent rate capacities came from the high ratio of the capacitive contribution.

2.3. Full-cell Behaviors of Flexible Asymmetric Supercapacitor. To further demonstrate the practical application of CF@NiCoO$_2$@N−C, an asymmetric supercapacitor was fabricated. The as-prepared CF@NiCoO$_2$@N−C was used as the cathode, CF@N−C nanowires were used as the anode, and polyvinyl alcohol (PVA)/KOH was used as the solid electrolyte (Figure 4a). The anode of CF@N−C was prepared via a similar electrodeposition method, obtaining a uniform nanowire structure according to the SEM image (Figure S6). The CF@N−C showed outstanding electric double-layer behavior in CV curves from −1.0 to 0 V (Figure S7), and GCD measurements were obtained at different current densities to estimate the capacitances of the CF@N−C anode (Figure S8). The combined CV curves of CF@NiCoO$_2$@N−C and CF@N−C are shown in Figure 4b, demonstrating the appropriate voltage window of the flexible asymmetric supercapacitor (FASC) to be −1 to 0 V and 0−0.6 V, respectively. Furthermore, the voltage window of the as-fabricated FASC was evaluated in the range of 0−1 and 0−1.6 V from CV curves (Figure 4c), and there was no obvious

https://dx.doi.org/10.1021/acsami.0c05465
ACS Appl. Mater. Interfaces 2020, 12, 21779−21787

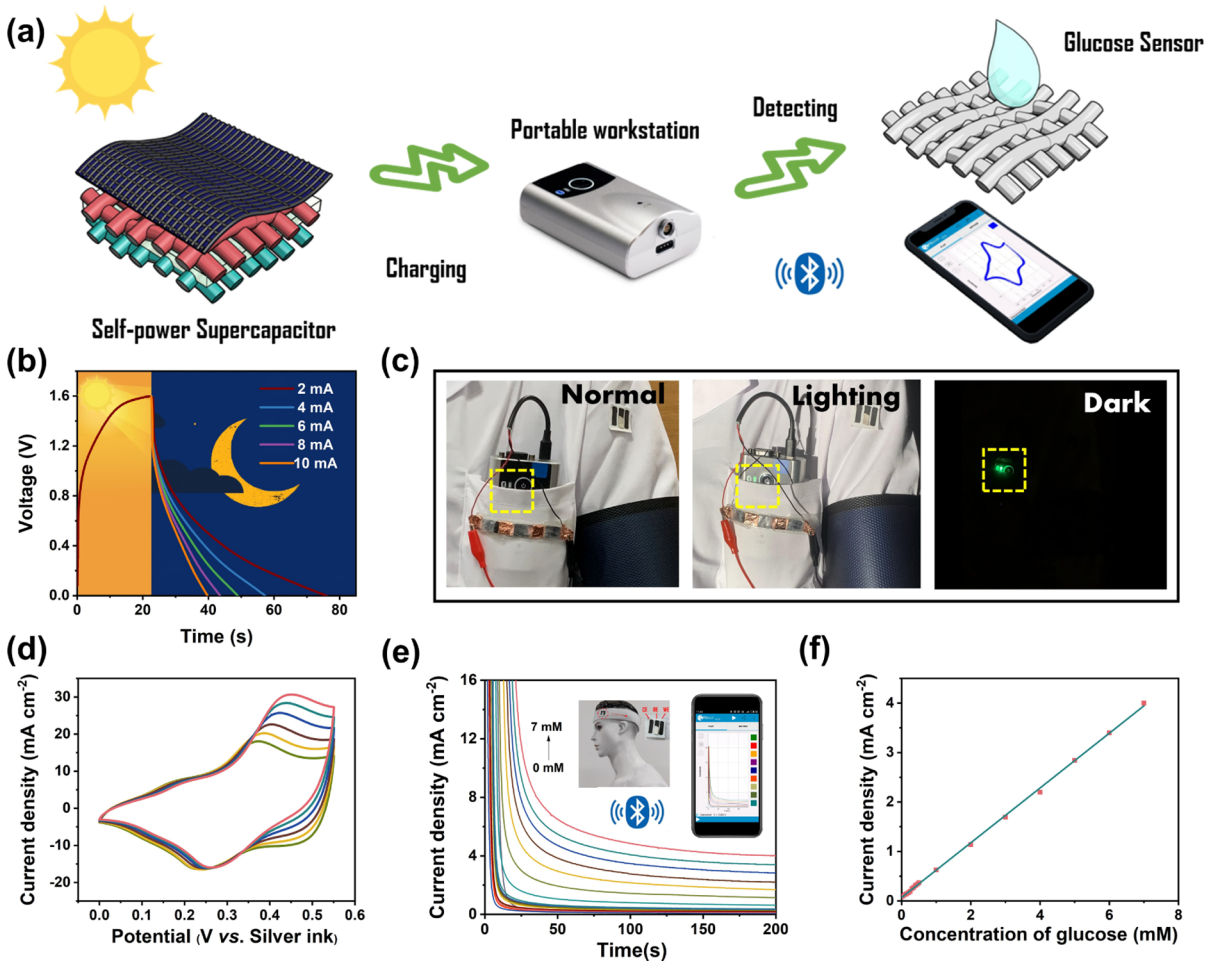

Figure 5. (a) Schematic illustration of a wearable FASC for a self-powered glucose smartsensor system. (b) GCD curves of the self-powered three FASCs in series, charging and discharging in a simulative sunlight or a dark environment. (c) Digital photos of the self-powered FASC driving the portable workstation at different states. (d) CV curves of the CF@$NiCoO_2$@N−C-based glucose sensor in the concentration range of 0−5 mM at 20 mV s^{-1}. (e) Amperometric *i*−*t* curves of the wearable FASC for the self-powered glucose smartsensor in the concentration range of 0−7 mM, the insets are the photographs of the wearable glucose sensor in the headband operated using a smartphone. (f) The Linear relationship of the glucose concentration collected at 200 s from (e).

polarization in the measured potential range. Thus, the safety voltage window was set to be 0−1.6 V for the device of FASC. The FASC at various scan rates exhibited an ideal capacitive behavior with satisfying reversibility (Figure 4d). Meanwhile, the specific capacitance was measured to be 98.5 mF cm^{-2} at 2 mA cm^{-2} from the GCD curves (Figure 4e). The thickness of the ASCs measured with a micrometer was about 0.86 mm (Figure S9), and the volume capacitance was 1145 mF cm^{-3} at 2 mA cm^{-2} (Figure S10). EIS of the assembled hybrid supercapacitor has been measured (Figure 4f), and the equivalent electrical circuit is shown in the inset. The equivalent series resistance was as low as 3.1 Ω, resulting from fast ion transfer between the active materials and the electrolyte.

Moreover, the FASC shows good electrochemical stability, the specific capacitance of the FASC was maintained 95% even after 8000 cycles (Figure 4g). The DUT (Dalian University of Technology) light-emitting diode (LED) was powered using three serially connected FASCs as shown in the inset of Figure 4g. In addition, the FASC exhibited excellent flexible and wearable behaviors during bending and twisting testing (Figure 4h). In the case of numerous bending cycles of the FASC, 95% capacitance was maintained even after 10,000 cycles (Figure 4i). The fabricated FASC device exhibited outstanding mechanical stability and flexibility for powering future smart wearable sensors and electronics.

2.4. FASC for Self-Powered Enzyme-Free Smartsensors. For a wider practical application of flexible supercapacitors, a wearable self-powered enzyme-free smartsensor system has been designed in this work (Figure 5a). First, solar cells convert sunlight into electric energy for storing in supercapacitors. Furthermore, the self-powered energy devices can power portable workstations, bluetooth modules, and wireless transmitters used for detecting glucose. Moreover, the response signal can be wirelessly transmitted to a smartphone via bluetooth for achieving remote control. The flow chart of the integrated system shown in Figure S11 explains the working process. Interestingly, the as-prepared CF@$NiCoO_2$@N−C could be used as a dual-functional active material, both the cathode material in flexible supercapacitors and the wearable enzyme-free electrode in biosensors. Combining with the bluetooth technology, the as-prepared CF@$NiCoO_2$@N−C-based wearable FASC for self-powered enzyme-free sensors could be remotely controlled using a smartphone. The flexible solar cells were used as energy harvesting devices to produce electricity from sunlight, and

https://dx.doi.org/10.1021/acsami.0c05465
ACS Appl. Mater. Interfaces 2020, 12, 21779−21787

further can be connected with the as-obtained FASC to store energy with a low power consumption.

Solar cells were first exposed to sunlight, and then further fully charged the FASC continuously. The practical operation of the self-powered FASC has been demonstrated either in a light or dark environment for GCD measurement (Figure 5b). The FASC was first charged by solar cells under the light illumination, when switching into a dark environment, the FASC exhibited excellent discharge behaviors for 53.8, 35.0, 26.7, 21.2, and 17.5 s at 2, 4, 6, 8, and 10 mA cm^{-2}, respectively. Meanwhile, a portable workstation and a bluetooth module could be powered using three serially connected FASCs (Figure 5c and Movie S1), providing a feasible system for remote detection using non-enzymatic biosensors.

To demonstrate the biosensing performance of the as-prepared CF@$NiCoO_2$@N−C, the CV curves for electrocatalytic glucose monitoring (0−5 mM) have been obtained and are shown in Figure 5d. Upon increasing the concentration of glucose, well-defined electrocatalysis occurred starting at 0.45 V (vs Sliver ink), and the electrocatalytic current proportionally increased. During the electrochemical process, glucose was oxidized to gluconolactone by CF@$NiCoO_2$@N−C, while Co(IV) and Ni(III) were reduced into Co(III) and Ni(II), respectively. The reaction processes were depicted in eqs 7, 8, and 9.[35,36,51]

$$NiCoO_2 + 2OH^- \rightarrow NiOOH + CoOOH + 2e^- \quad (7)$$

$$NiOOH + glucose \rightarrow Ni(OH)_2 + glucolactone \quad (8)$$

$$CoOOH + OH^- \rightarrow CoO_2 + H_2O + e^- \quad (9)$$

$$CoO_2 + glucose \rightarrow CoOOH + glucolactone \quad (10)$$

When assembling the FASC for a wearable self-powered wireless glucose sensor via smartphone remote control, electrochemical signals demonstrated good sensing properties between the response of current and the glucose concentration displaying on the smartphone according to the amperometry (i−t) curves (Figure 5e), corresponding to the concentration of glucose from 0 to 7 mM. An excellent linear relationship between current density and glucose concentration was also obtained, with a sensitivity of 592 μA mM^{-1} and a detection limit of 34.8 μM (Figure 5f), which are superior electrochemical behaviors compared with those of the state-of-the-art devices reported in the literature (Table S1). The high sensitivity for glucose can be attributed to the significant electrochemical properties of CF@$NiCoO_2$@N−C.

3. CONCLUSIONS

In conclusion, we have successfully fabricated a wearable FASC for a self-powered smartsensor system based on the dual-functional CF@$NiCoO_2$@N−C material. Thanks to the successful preparation of the CF@$NiCoO_2$@N−C electrode, achieving a high capacitance of 644.29 mF cm^{-2} and an outstanding stability 93.7% after 10,000 cycles. Moreover, the as-prepared FASC also showed great electrochemical performance and excellent flexible stability, because of the CF@N−C electrode and the PVA/KOH gel electrolyte. As wearable devices, FASCs maintained 95% capacitance even after 8000 cycles and 10,000 bending cycles, showing their potential to be applied in wearable systems. Meanwhile, the CF@$NiCoO_2$@N−C-based glucose sensors exhibited a high sensitivity of 0.62 mA mM^{-1}, suitable for real-time body biomolecule detection. The FASC and the glucose sensors were integrated with flexible solar cells and bluetooth into a wearable self-powered smartsensor system, achieving excellent biosensing performance. As a prospective study, the present work shows promise for developing integrated, highly stable wearable self-powered smartsensor systems for energy harvesting, energy storage, and detection of biomolecules.

4. MATERIALS AND METHODS

4.1. Preparation of CF@$NiCoO_2$@N−C Electrodes. Typically, the carbon fiber (CF) substrate (1 cm × 2 cm) was first pretreated with absolute deionized water, ethanol, and acetone (each for 15 min) to ensure a clean surface, and then placed in nitric acid for 12 h at 80 °C. Second, electrochemical deposition of the CF was carried out by potentiostatic deposition for 100 s at a potential of −1 V *vs* the saturated calomel electrode (SCE) in a three-electrode system, with Pt foil as the counter electrode in the 0.15 M $CoCl_2$ and 0.15 M $Ni(NO_3)_2$ mixed aqueous electrolyte. After washing with deionized water and then drying in a vacuum oven overnight (60 °C), another potentiostatic deposition was carried out for 50 s at a potential of 0.9 V *vs* the SCE in the electrolyte of PPy, obtained by mixing 0.15 M PPy, 0.2 M Na_2HPO_4, and 0.0015 M $NaClO_4$. The resulting CF@NiCo-precursor@PPy electrodes were rinsed with distilled water, and dried in a vacuum oven overnight (60 °C). Third, a piece of CF@NiCo-precursor@PPy was annealed in an Ar atmosphere at 450 °C for 2 h with a ramp rate of 5 °C min^{-1}. Finally, the CF@$NiCoO_2$@N−C electrode was obtained.

4.2. Preparation of CF@N−C Electrodes. The preparation process was similar to the previous step of electrodepositing PPy directly on the CF. In short, the potentiostatic deposition was carried out for 1.5 h at a potential of 0.9 V *vs* SCE. The CF@N−C electrode was achieved after annealing in an Ar atmosphere at 450 °C for 2 h with a ramp rate of 5 °C min^{-1}.

4.3. Assembling of a Self-Powered Flexible Glucose-Sensing System. First, a FASC was fabricated using the as-prepared CF@$NiCoO_2$@N−C and CF@N−C with the PVA/KOH gel electrolyte, as the positive and negative electrode, respectively. Typically, 6 g PVA was dissolved in 50 mL deionized water, and slowly heated in a 90 °C water bath with continuous stirring for 2 h. Then, the KOH solution (3.36 g KOH into 10 mL deionized water) was dropped into the PVA gel solution under continuous stirring until a clear solution was obtained. As a result, the FASC was assembled by CF@$NiCoO_2$@N−C, CF@N−C, and PVA/KOH on non-woven fabrics. Then, self-powered energy devices were combined the three serially connected FASCs with a flexible solar cell (amorphous silicon, brought from NESolar). Enzyme-free glucose sensors were fabricated as follows, this sensor included a working electrode (WE), a reference electrode (RE), and a counter electrode (CE). Here, the CF@$NiCoO_2$@N−C electrode and the untreated CF were used as the WE and CE, the sliver ink-coated CF was cured at 60 °C for 30 min as the RE. Moreover, three electrodes could be integrated into one piece of textile fabrics. Finally, a self-powered flexible glucose-sensing system was obtained, and it directly drives a portable wireless workstation for sensing glucose.

4.4. Characterization. The powder XRD measurement was carried out using a X-ray diffractometer (SmartLab, Rigaku). Scanning electron microscopy images (SEM) and elemental maps were obtained on a field emission scanning electron microscope (SU8220, Hitachi) equipped with an energy dispersive X-ray spectrometer (EDS). TEM was performed using a Philips Tecnai G2F20. XPS measurement was performed on an X-ray photoelectron spectrometer (ESCALAB XI+, Thermo).

4.5. Electrochemical Measurements. The electrochemical measurements including cyclic voltammetry (CV), GCD, EIS, and amperometry (i−t) were performed using an electrochemical working station (CHI 660E) with a typical three-electrode system at room temperature with 1 M KOH aqueous solution, and Pt foil and a Hg/HgO electrode were used as the CE and the RE, respectively.

https://dx.doi.org/10.1021/acsami.0c05465
ACS Appl. Mater. Interfaces 2020, 12, 21779−21787

■ ASSOCIATED CONTENT

Supporting Information

The Supporting Information is available free of charge at https://pubs.acs.org/doi/10.1021/acsami.0c05465.

SEM images of CF@N−C and CF@$NiCoO_2$; EIS data of CF@$NiCoO_2$ and CF@$NiCoO_2$@N−C; CV curves of CF@N−C at different scan rates; and GCD curves of CF@N−C at different current densities (PDF)

Working demonstration of the device under light and dark conditions (MP4)

■ AUTHOR INFORMATION

Corresponding Author

Nan Zhu − *Zhang Dayu School of Chemistry, Dalian University of Technology, Dalian, Liaoning 116024, China;* orcid.org/0000-0001-6029-6200; Email: nanzhu@dlut.edu.cn

Authors

Tongrui Sun − *Zhang Dayu School of Chemistry, Dalian University of Technology, Dalian, Liaoning 116024, China*

Liuxue Shen − *Zhang Dayu School of Chemistry, Dalian University of Technology, Dalian, Liaoning 116024, China*

Yu Jiang − *Zhang Dayu School of Chemistry, Dalian University of Technology, Dalian, Liaoning 116024, China*

Junlin Ma − *Zhang Dayu School of Chemistry, Dalian University of Technology, Dalian, Liaoning 116024, China*

Fengjuan Lv − *Zhang Dayu School of Chemistry, Dalian University of Technology, Dalian, Liaoning 116024, China*

Hongting Ma − *Zhang Dayu School of Chemistry, Dalian University of Technology, Dalian, Liaoning 116024, China*

Dawei Chen − *Neware Technology Limited, Shenzhen, Guangdong 518049, China*

Complete contact information is available at: https://pubs.acs.org/10.1021/acsami.0c05465

Author Contributions

§T.S. and L.S. contributed equally.

Notes

The authors declare no competing financial interest.

■ ACKNOWLEDGMENTS

We are grateful for the financial support from the National Natural Science Foundation of China (grant no. 21705014), the Fundamental Research Funds for Central Universities (grant no. DUT18LK56), Natural Science Foundation of Liaoning Province, China (grant no.20180510060), Dalian Science and Technology Bureau, China (grant no. 2019J12SN54), and Zhang Dayu School of Chemistry, Dalian University of Technology, China.

■ REFERENCES

(1) Kim, J.; Campbell, A. S.; de Ávila, B. E.-F.; Wang, J. Wearable Biosensors for Healthcare Monitoring. *Nat. Biotechnol.* **2019**, *37*, 389−406.

(2) Ciui, B.; Martin, A.; Mishra, R. K.; Nakagawa, T.; Dawkins, T. J.; Lyu, M.; Cristea, C.; Sandulescu, R.; Wang, J. Chemical Sensing at the Robot Fingertips: Toward Automated Taste Discrimination in Food Samples. *ACS Sens.* **2018**, *3*, 2375−2384.

(3) Zhang, Q.; Liang, Q.; Zhang, Z.; Kang, Z.; Liao, Q.; Ding, Y.; Ma, M.; Gao, F.; Zhao, X.; Zhang, Y. Electromagnetic Shielding Hybrid Nanogenerator for Health Monitoring and Protection. *Adv. Funct. Mater.* **2018**, *28*, 1703801.

(4) Jiang, Y.; Ma, J.; Lv, J.; Ma, H.; Xia, H.; Wang, J.; Yang, C.; Xue, M.; Li, G.; Zhu, N. Facile Wearable Vapor/Liquid Amphibious Methanol Sensor. *ACS Sens.* **2019**, *4*, 152−160.

(5) Lu, Y.; Jiang, K.; Chen, D.; Shen, G. Wearable Sweat Monitoring System with Integrated Micro-Supercapacitors. *Nano Energy* **2019**, *58*, 624−632.

(6) Ma, J.; Jiang, Y.; Shen, L.; Ma, H.; Sun, T.; Lv, F.; Kiran, A.; Zhu, N. Wearable Biomolecule Smartsensors Based on One-Step Fabricated Berlin Green Printed Arrays. *Biosens. Bioelectron.* **2019**, *144*, 111637.

(7) Gao, W.; Emaminejad, S.; Nyein, H. Y. Y.; Challa, S.; Chen, K.; Peck, A.; Fahad, H. M.; Ota, H.; Shiraki, H.; Kiriya, D.; Lien, D.-H.; Brooks, G. A.; Davis, R. W.; Javey, A. Fully Integrated Wearable Sensor Arrays for Multiplexed in Situ Perspiration Analysis. *Nature* **2016**, *529*, 509−514.

(8) Sun, P.; Qiu, M.; Li, M.; Mai, W.; Cui, G.; Tong, Y. Stretchable Ni@Nicop Textile for Wearable Energy Storage Clothes. *Nano Energy* **2019**, *55*, 506−515.

(9) Shen, L.; Du, L.; Tan, S.; Zang, Z.; Zhao, C.; Mai, W. Flexible Electrochromic Supercapacitor Hybrid Electrodes Based on Tungsten Oxide Films and Silver Nanowires. *Chem. Commun.* **2016**, *52*, 6296−6299.

(10) Choi, C.; Kim, K. M.; Kim, K. J.; Lepro, X.; Spinks, G. M.; Baughman, R. H.; Kim, S. J. Improvement of System Capacitance Via Weavable Superelastic Biscrolled Yarn Supercapacitors. *Nat. Commun.* **2016**, *7*, 13811.

(11) Yang, Y.; Huang, Q.; Niu, L.; Wang, D.; Yan, C.; She, Y.; Zheng, Z. . Waterproof, Ultrahigh Areal-Capacitance, Wearable Supercapacitor Fabrics. *Adv. Mater.* **2017**, *29*, 1606679.

(12) Yu, K.-H.; Beam, A. L.; Kohane, I. S. Artificial Intelligence in Healthcare. *Nat. Biomed. Eng.* **2018**, *2*, 719−731.

(13) Palmstrom, A. F.; Eperon, G. E.; Leijtens, T.; Prasanna, R.; Habisreutinger, S. N.; Nemeth, W.; Gaulding, E. A.; Dunfield, S. P.; Reese, M.; Nanayakkara, S.; Moot, T.; Werner, J.; Liu, J.; To, B.; Christensen, S. T.; McGehee, M. D.; van Hest, M. F. A. M.; Luther, J. M.; Berry, J. J.; Moore, D. T. Enabling Flexible All-Perovskite Tandem Solar Cells. *Joule* **2019**, *3*, 2193−2204.

(14) Dagdeviren, C.; Javid, F.; Joe, P.; von Erlach, T.; Bensel, T.; Wei, Z.; Saxton, S.; Cleveland, C.; Booth, L.; McDonnell, S.; Collins, J.; Hayward, A.; Langer, R.; Traverso, G. Flexible Piezoelectric Devices for Gastrointestinal Motility Sensing. *Nat. Biomed. Eng.* **2017**, *1*, 807−817.

(15) He, X.; Zi, Y.; Guo, H.; Zheng, H.; Xi, Y.; Wu, C.; Wang, J.; Zhang, W.; Lu, C.; Wang, Z. L. A Highly Stretchable Fiber-Based Triboelectric Nanogenerator for Self-Powered Wearable Electronics. *Adv. Funct. Mater.* **2017**, *27*, 1604378.

(16) Shi, X.; Wu, Z. S.; Qin, J.; Zheng, S.; Wang, S.; Zhou, F.; Sun, C.; Bao, X. Graphene-Based Linear Tandem Micro-Supercapacitors with Metal-Free Current Collectors and High-Voltage Output. *Adv. Mater.* **2017**, *29*, 1703034.

(17) Couly, C.; Alhabeb, M.; Van Aken, K. L.; Kurra, N.; Gomes, L.; Navarro-Suárez, A. M.; Anasori, B.; Alshareef, H. N.; Gogotsi, Y. Asymmetric Flexible Mxene-Reduced Graphene Oxide Micro-Supercapacitor. *Adv. Electron. Mater.* **2018**, *4*, 1700339.

(18) Qiu, M.; Sun, P.; Cui, G.; Tong, Y.; Mai, W. A Flexible Microsupercapacitor with Integral Photocatalytic Fuel Cell for Self-Charging. *ACS Nano* **2019**, *13*, 8246−8255.

(19) Anothumakkool, B.; Soni, R.; Bhange, S. N.; Kurungot, S. Novel Scalable Synthesis of Highly Conducting and Robust Pedot Paper for a High Performance Flexible Solid Supercapacitor. *Energy Environ. Sci.* **2015**, *8*, 1339−1347.

(20) Liao, Q.; Li, N.; Jin, S.; Yang, G.; Wang, C. All-Solid-State Symmetric Supercapacitor Based on Co3o4 Nanoparticles on Vertically Aligned Graphene. *ACS Nano* **2015**, *9*, 5310−5317.

(21) Qin, T.; Peng, S.; Hao, J.; Wen, Y.; Wang, Z.; Wang, X.; He, D.; Zhang, J.; Hou, J.; Cao, G. Flexible and Wearable All-Solid-State Supercapacitors with Ultrahigh Energy Density Based on a Carbon Fiber Fabric Electrode. *Adv. Energy Mater.* **2017**, *7*, 1700409.

(22) Yang, P.; Mai, W. Flexible Solid-State Electrochemical Supercapacitors. *Nano Energy* **2014**, *8*, 274−290.
(23) Yuan, Y.; Lu, Y.; Jia, B. E.; Tang, H.; Chen, L.; Zeng, Y. J.; Hou, Y.; Zhang, Q.; He, Q.; Jiao, L.; Leng, J.; Ye, Z.; Lu, J. Integrated System of Solar Cells with Hierarchical Nico2o4 Battery-Supercapacitor Hybrid Devices for Self-Driving Light-Emitting Diodes. *Nano-Micro Lett.* **2019**, *11*, 42.
(24) Liu, Z.; Zhong, Y.; Sun, B.; Liu, X.; Han, J.; Shi, T.; Tang, Z.; Liao, G. Novel Integration of Perovskite Solar Cell and Supercapacitor Based on Carbon Electrode for Hybridizing Energy Conversion and Storage. *ACS Appl. Mater. Interfaces* **2017**, *9*, 22361−22368.
(25) Yuan, Y.; Wu, Y.; Zhang, T.; Tang, H.; Meng, L.; Zeng, Y.-J.; Zhang, Q.; Ye, Z.; Lu, J. Integration of Solar Cells with Hierarchical Cos Nanonets Hybrid Supercapacitors for Self-Powered Photodetection Systems. *J. Power Sources* **2018**, *404*, 118−125.
(26) Manjakkal, L.; Núñez, C. G.; Dang, W.; Dahiya, R. Flexible Self-Charging Supercapacitor Based on Graphene-Ag-3d Graphene Foam Electrodes. *Nano Energy* **2018**, *51*, 604−612.
(27) Li, B.; Dai, F.; Xiao, Q.; Yang, L.; Shen, J.; Zhang, C.; Cai, M. Nitrogen-Doped Activated Carbon for a High Energy Hybrid Supercapacitor. *Energy Environ. Sci.* **2016**, *9*, 102−106.
(28) Lu, Y.; Zhang, S.; Yin, J.; Bai, C.; Zhang, J.; Li, Y.; Yang, Y.; Ge, Z.; Zhang, M.; Wei, L.; Ma, M.; Ma, Y.; Chen, Y. Mesoporous Activated Carbon Materials with Ultrahigh Mesopore Volume and Effective Specific Surface Area for High Performance Supercapacitors. *Carbon* **2017**, *124*, 64−71.
(29) Wang, T.; Chen, H. C.; Yu, F.; Zhao, X. S.; Wang, H. Boosting the Cycling Stability of Transition Metal Compounds-Based Supercapacitors. *Energy Storage Mater.* **2019**, *16*, 545−573.
(30) Pomerantseva, E.; Bonaccorso, F.; Feng, X.; Cui, Y.; Gogotsi, Y. Energy Storage: The Future Enabled by Nanomaterials. *Science* **2019**, *366*, No. eaan8285.
(31) Yu, N.; Yin, H.; Zhang, W.; Liu, Y.; Tang, Z.; Zhu, M. Q. High-Performance Fiber-Shaped All-Solid-State Asymmetric Supercapacitors Based on Ultrathin Mno2nanosheet/Carbon Fiber Cathodes for Wearable Electronics. *Adv. Energy Mater.* **2016**, *6*, 1501458.
(32) Nayak, A. K.; Das, A. K.; Pradhan, D. High Performance Solid-State Asymmetric Supercapacitor using Green Synthesized Graphene-WO3 Nanowires Nanocomposite. *ACS Sustainable Chem. Eng.* **2017**, *5*, 10128−10138.
(33) Xu, Y.; Wei, J.; Tan, L.; Yu, J.; Chen, Y. A Facile Approach to Nicoo2 Intimately Standing on Nitrogen Doped Graphene Sheets by One-Step Hydrothermal Synthesis for Supercapacitors. *J. Mater. Chem. A* **2015**, *3*, 7121−7131.
(34) Huang, Z.-D.; Zhang, K.; Zhang, T.-T.; Yang, X.-S.; Liu, R.-Q.; Li, Y.; Lin, X.-J.; Feng, X.-M.; Ma, Y.-W.; Huang, W. Hierarchical Nicoo 2 Mesoporous Microspheres as Anode for Lithium Ion Batteries with Superior Rate Capability. *Energy Storage Mater.* **2016**, *3*, 36−44.
(35) Yu, Z.; Li, H.; Zhang, X.; Liu, N.; Tan, W.; Zhang, X.; Zhang, L. Facile Synthesis of Nico2o4@Polyaniline Core-Shell Nanocomposite for Sensitive Determination of Glucose. *Biosens. Bioelectron.* **2016**, *75*, 161−165.
(36) Tang, X.; Zhang, B.; Xiao, C.; Zhou, H.; Wang, X.; He, D. Carbon Nanotube Template Synthesis of Hierarchical Nicoo2 Composite for Non-Enzyme Glucose Detection. *Sens. Actuators, B* **2016**, *222*, 232−239.
(37) Guo, D.; Qin, J.; Yin, Z.; Bai, J.; Sun, Y.-K.; Cao, M. Achieving High Mass Loading of Na3v2(Po4)3@Carbon on Carbon Cloth by Constructing Three-Dimensional Network between Carbon Fibers for Ultralong Cycle-Life and Ultrahigh Rate Sodium-Ion Batteries. *Nano Energy* **2018**, *45*, 136−147.
(38) Liang, J.; Xi, K.; Tan, G.; Chen, S.; Zhao, T.; Coxon, P. R.; Kim, H.-K.; Ding, S.; Yang, Y.; Kumar, R. V.; Lu, J. Sea Urchin-Like Nicoo2@C Nanocomposites for Li-Ion Batteries and Supercapacitors. *Nano Energy* **2016**, *27*, 457−465.
(39) Luo, W.; Li, F.; Gaumet, J. J.; Magri, P.; Diliberto, S.; Zhou, L.; Mai, L. Bottom-up Confined Synthesis of Nanorod-in-Nanotube Structured Sb@N-C for Durable Lithium and Sodium Storage. *Adv. Energy Mater.* **2018**, *8*, 1703237.
(40) Zhu, J.; Xu, Y.; Zhang, Y.; Feng, T.; Wang, J.; Mao, S.; Xiong, L. Porous and High Electronic Conductivity Nitrogen-Doped Nano-Sheet Carbon Derived from Polypyrrole for High-Power Supercapacitors. *Carbon* **2016**, *107*, 638−645.
(41) Wang, Q.; Wang, X.; Xu, J.; Ouyang, X.; Hou, X.; Chen, D.; Wang, R.; Shen, G. Flexible Coaxial-Type Fiber Supercapacitor Based on Nico2o4 Nanosheets Electrodes. *Nano Energy* **2014**, *8*, 44−51.
(42) Qian, Y.; Liu, R.; Wang, Q.; Xu, J.; Chen, D.; Shen, G. Efficient Synthesis of Hierarchical Nio Nanosheets for High-Performance Flexible All-Solid-State Supercapacitors. *J. Mater. Chem. A* **2014**, *2*, 10917−10922.
(43) Zhou, K.; Zhou, W.; Yang, L.; Lu, J.; Cheng, S.; Mai, W.; Tang, Z.; Li, L.; Chen, S. Ultrahigh-Performance Pseudocapacitor Electrodes Based on Transition Metal Phosphide Nanosheets Array Via Phosphorization: A General and Effective Approach. *Adv. Funct. Mater.* **2015**, *25*, 7530−7538.
(44) Ai, Y.; Geng, X.; Lou, Z.; Wang, Z. M.; Shen, G. Rational Synthesis of Branched Comoo4@Conio2 Core/Shell Nanowire Arrays for All-Solid-State Supercapacitors with Improved Performance. *ACS Appl. Mater. Interfaces* **2015**, *7*, 24204−24211.
(45) Rakhi, R. B.; Chen, W.; Cha, D.; Alshareef, H. N. Substrate Dependent Self-Organization of Mesoporous Cobalt Oxide Nanowires with Remarkable Pseudocapacitance. *Nano Lett.* **2012**, *12*, 2559−2567.
(46) Wang, H.; Holt, C. M. B.; Li, Z.; Tan, X.; Amirkhiz, B. S.; Xu, Z.; Olsen, B. C.; Stephenson, T.; Mitlin, D. Graphene-Nickel Cobaltite Nanocomposite Asymmetrical Supercapacitor with Commercial Level Mass Loading. *Nano Res.* **2012**, *5*, 605−617.
(47) Wang, J.; Polleux, J.; Lim, J.; Dunn, B. Pseudocapacitive Contributions to Electrochemical Energy Storage in Tio2(Anatase) Nanoparticles. *J. Phys. Chem. C* **2007**, *111*, 14925−14931.
(48) Purkait, T.; Dimple; Kamboj, N.; Das, M.; Sarkar, S.; De Sarkar, A.; Dey, R. S. Electrochemically Customized Assembly of a Hybrid Xerogel Material Via Combined Covalent and Non-Covalent Conjugation Chemistry: An Approach for Boosting the Cycling Performance of Pseudocapacitors. *J. Mater. Chem. A* **2020**, *8*, 6740−6756.
(49) Chao, D.; Zhu, C.; Yang, P.; Xia, X.; Liu, J.; Wang, J.; Fan, X.; Savilov, S. V.; Lin, J.; Fan, H. J.; Shen, Z. X. Array of Nanosheets Render Ultrafast and High-Capacity Na-Ion Storage by Tunable Pseudocapacitance. *Nat. Commun.* **2016**, *7*, 12122.
(50) Ge, P.; Zhang, C.; Hou, H.; Wu, B.; Zhou, L.; Li, S.; Wu, T.; Hu, J.; Mai, L.; Ji, X. Anions induced evolution of Co3X4 (X = O, S, Se) as sodium-ion anodes: The influences of electronic structure, morphology, electrochemical property. *Nano Energy* **2018**, *48*, 617−629.
(51) Ding, Y.; Wang, Y.; Su, L.; Bellagamba, M.; Zhang, H.; Lei, Y. Electrospun Co3o4 Nanofibers for Sensitive and Selective Glucose Detection. *Biosens. Bioelectron.* **2010**, *26*, 542−548.

https://dx.doi.org/10.1021/acsami.0c05465
ACS Appl. Mater. Interfaces 2020, 12, 21779−21787